Structural properties of Bi2− x Mn x Se3 thin films grown via molecular beam epitaxy

Sercan Babakiray, Trent A. Johnson, Pavel Borisov, Mikel B. Holcomb, David Lederman, Matthew A. Marcus, and Kartick Tarafder

---

Articles you may be interested in

X-ray magnetic spectroscopy of MBE-grown Mn-doped Bi2Se3 thin films
AIP Advances **4**, 127136 (2014); 10.1063/1.4904900

Domain formation due to surface steps in topological insulator Bi2Te3 thin films grown on Si (111) by molecular beam epitaxy
Appl. Phys. Lett. **103**, 081902 (2013); 10.1063/1.4818456

Two-step growth of high quality Bi2Te3 thin films on Al2O3 (0001) by molecular beam epitaxy
Appl. Phys. Lett. **102**, 171906 (2013); 10.1063/1.4803717

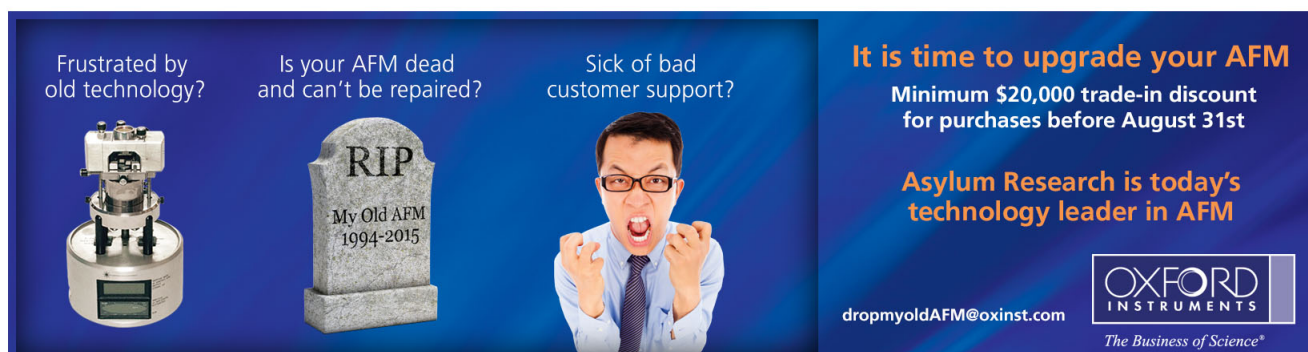Molecular beam epitaxy of high structural quality Bi2Se3 on lattice matched InP(111) substrates
Appl. Phys. Lett. **102**, 041914 (2013); 10.1063/1.4789775

Molecular beam epitaxy and characterization of thin Bi2Se3 films on Al2O3 (110)
Appl. Phys. Lett. **99**, 013111 (2011); 10.1063/1.3609326

Structural properties of $Bi_{2-x}Mn_xSe_3$ thin films grown via molecular beam epitaxy

Sercan Babakiray,[1] Trent A. Johnson,[1] Pavel Borisov,[1] Mikel B. Holcomb,[1] David Lederman,[1,a)] Matthew A. Marcus,[2] and Kartick Tarafder[3]

[1]*Department of Physics and Astronomy, West Virginia University, Morgantown, West Virginia 26506-6315, USA*
[2]*Advanced Light Source, Lawrence Berkeley National Laboratory, Berkeley, California 94720, USA*
[3]*Department of Physics, BITS-Pilani Hyderabad Campus, Secunderabad, Andhra Pradesh 500078, India*

The effects of Mn doping on the structural properties of the topological insulator Bi_2Se_3 in thin film form were studied in samples grown via molecular beam epitaxy. Extended x-ray absorption fine structure measurements, supported by density functional theory calculations, indicate that preferential incorporation occurs substitutionally in Bi sites across the entire film volume. This finding is consistent with x-ray diffraction measurements which show that the out of plane lattice constant expands while the in plane lattice constant contracts as the Mn concentration is increased. X-ray photoelectron spectroscopy indicates that the Mn valency is 2+ and that the Mn bonding is similar to that in MnSe. The expansion along the out of plane direction is most likely due to weakening of the Van der Waals interactions between adjacent Se planes. Transport measurements are consistent with this Mn^{2+} substitution of Bi sites if additional structural defects induced by this substitution are taken into account. © 2015 AIP Publishing LLC. [http://dx.doi.org/10.1063/1.4927171]

I. INTRODUCTION

Topological insulators (TIs) are a new class of quantum matter with a bulk band gap and gapless metallic surface states.[1–3] The spin and momentum degrees of freedom are locked and are robust against non-magnetic perturbations. The surface states of a three dimensional (3D) topological insulator were first observed in $Bi_{1-x}Sb_x$ with a Dirac-like energy momentum dispersion relation.[4] The surface-sensitive techniques angle resolved photoemission spectroscopy (ARPES) and spin and angle resolved photoemission spectroscopy (SARPES) have been used to confirm the band structure of the surface states.[4–6]

Among the known 3D TI materials, Bi_2Se_3 has a relatively large band gap of ~ 0.3 eV.[7] The effect of magnetic impurities in this material has been investigated experimentally and computationally in nanoribbons, thin films, and single crystals doped with ferrocene,[8] Cr,[9,10] Fe,[11] and Mn.[12] For the case of Mn-doped Bi_2Se_3 single crystals[12] and thin films,[13–15] the experimental research has focused almost exclusively on the carrier type conversion in the electrical transport and the magnetization properties with an emphasis on ferromagnetism. In particular, Zhang *et al.* describe the transition of weak anti-localization to weak localization with increasing Mn concentration[14] using a modified Hikami-Larkin-Nagaoka (HLN) transport model[16] that takes into account the opening of an energy gap in the topological states' dispersion relation due to the presence of magnetic impurities.[17] However, the samples used in Ref. 14 had a higher concentration of Mn at the surface than in the bulk, and the carrier density was reported to increase with

increasing Mn concentration. An increase in *n*-type carrier density is not expected if Mn is substitutionally incorporated for Bi, because the Mn valency could either be 3+ (the same as Bi^{3+}), as predicted by density functional theory (DFT),[18] or 2+ if bonding is of the MnSe type (NaCl crystal structure).[19] In the latter case, Mn impurities would act as acceptors and thus decrease, not increase, the carrier density due to partial carrier compensation.

Here we present a systematic study of the structural properties of Mn-doped Bi_2Se_3 thin films grown by molecular beam epitaxy (MBE). X-ray photoelectron spectroscopy (XPS) data indicate that Mn is incorporated into the lattice with a valency similar to that of MnSe (2+). Using extended x-ray absorption fine structure (EXAFS) measurements, we show that the Mn is incorporated substitutionally into the Bi sites and that the distance to Se nearest neighbors is significantly smaller than the Bi-Se interatomic distance. X-ray diffraction (XRD) data indicate that a lattice expansion along the [001] direction parallel to the growth direction (using a hexagonal basis), as a function of Mn concentration, also observed in Cr-doped Bi_2Se_3 thin films, is accompanied by a decrease in the lattice constant in the plane of the sample. These measurements are consistent with the EXAFS data if Mn weakens the van der Waals bonding between adjacent Se planes. The variations of carrier density and mobility at low temperature as functions of Mn concentration are consistent with the structural characterization, including the Mn valency.

II. EXPERIMENTAL PROCEDURES

$Bi_{2-x}Mn_xSe_3$ thin films with approximate thicknesses of ~ 30 quintuple layers (QLs, 1 QL ≈ 0.95 nm) were grown on Al_2O_3 (0001) substrates by MBE in an ultra-high vacuum

a)Author to whom correspondence should be addressed. Electronic mail: david.lederman@mail.wvu.edu

118, 045302-1

chamber with a base pressure $P \approx 3.7 \times 10^{-10}$ Torr. Prior to the growth, the substrates were annealed in air for 2 h at 1200 °C to achieve an atomically smooth surface, as verified by atomic force microscopy (AFM). Bi (99.999%), Se (99.999%), and Mn (99.999%) were simultaneously evaporated using commercial Knudsen cells. Samples with Mn concentrations $x = 0$, 0.024, 0.047, 0.063 were grown. Material fluxes of the constituent Bi, Se, and Mn were measured using a quartz crystal monitor placed at the position of the substrate holder. The growth rate was determined by the Bi flux and kept at 0.6 QL/min. The growth was performed in two steps:[20] the first 3 QLs were grown at a substrate temperature of $T_S = 140$ °C, while the subsequent ones were grown after the substrate temperature was raised to $T_S = 275$ °C. The film surface quality was monitored *in-situ* using Reflection High-Energy Electron Diffraction (RHEED). Although RHEED oscillations were observed during the growth of pure ($x = 0$) Bi_2Se_3 films, indicating quintuple layer-by-layer growth, oscillations were not observed for samples with $x > 0$. The typical Se/Bi molar flux ratio value was 15 ± 0.7.[21] To avoid oxidation due to exposure to air, all samples were transferred to another growth chamber, without breaking vacuum, where they were capped with a 10 nm thick polycrystalline MgF_2 layer grown at room temperature by electron beam evaporation.[22] An additional sample with $x = 0.13$, 12 QL layers thick, was grown using the same conditions described above for XPS measurements in order to calibrate the Mn concentration and to determine the valency of the Mn impurities.

XPS depth profile analysis was performed using a Physical Electronics PHI 5000 VersaProbe XPS system with a monochromatic Al Kα source (energy $= 1486.7$ eV) and a beam diameter of approximately 100 μm equipped with a hemispherical detector oriented at a 45° take-off angle with respect to the sample surface. The MgF_2 capping layer was sputtered off using Ar ions with an energy of 2 keV and a current of 10 μA for 6 s intervals. Between each interval, survey scans from 0 eV to 1400 eV were performed. This was repeated until the Mg 1s and F 1s peaks almost disappeared. Once this was done, detailed scans of the Bi 4f, Se 3d, and Mn 2p transitions were acquired. The binding energies were calibrated to the C 1s peak coming from the surface of the sample before sputtering.

The crystal structure was analyzed using XRD and film thickness and interface roughness parameters were determined from x-ray reflectivity (XRR) measurements using the GenX software package.[23] X-ray scattering was measured using a Rigaku Cu rotating anode source and a bent crystal monochromator tuned to the Cu Kα radiation (0.15418 nm wavelength). XRD and XRR were measured on separate ports using four-circle and two-circle Huber goniometers, respectively. Surface topography was characterized by AFM using a Veeco Multimode scanning probe microscope.

In order to characterize the Mn impurity sites, x-ray absorption data were taken on the $x = 0.063$ sample at Advanced Light Source (ALS) beamline 10.3.2 at the Mn K-edge.[24] The sample was set to a 2° grazing angle with respect to the beam in order to increase the signal from the

thin $Bi_{2-x}Mn_xSe_3$ layer. The beam spot in the horizontal configuration was 12 μm in diameter, making the footprint on the sample 350 μm wide. The fluorescence signal was detected using an AmpTek drift-diode detector. The data were taken out to $k = 11.4$ Å^{-1}.

Prior to the transport measurements, the films were photolithographically etched into well-defined conduction paths. Linear resistivity and Hall effect signals were measured using a six-probe configuration in a Physical Property Measurement System (PPMS) from Quantum Design with the magnetic field applied perpendicular to the thin film surface. Electrical contacts were made using silver paste cured at room temperature.

III. RESULTS AND DISCUSSION

A. General structural characteristics

Figure 1(a) shows a typical RHEED image of the surface of the $x = 0.047$ film taken after the film growth. Streaky RHEED patterns confirmed the formation of an epitaxial film with a relatively smooth surface. All samples had similar RHEED patterns.

Images of the surface topography obtained from the top of the MgF_2 capping layers, such as the one shown in Fig. 1(b) for the $x = 0.047$ sample, had triangular structure which were likely related to the underlying $Bi_{2-x}Mn_xSe_3$ layer. The root mean square (RMS) surface roughness from the image was calculated to be 3.8 nm.
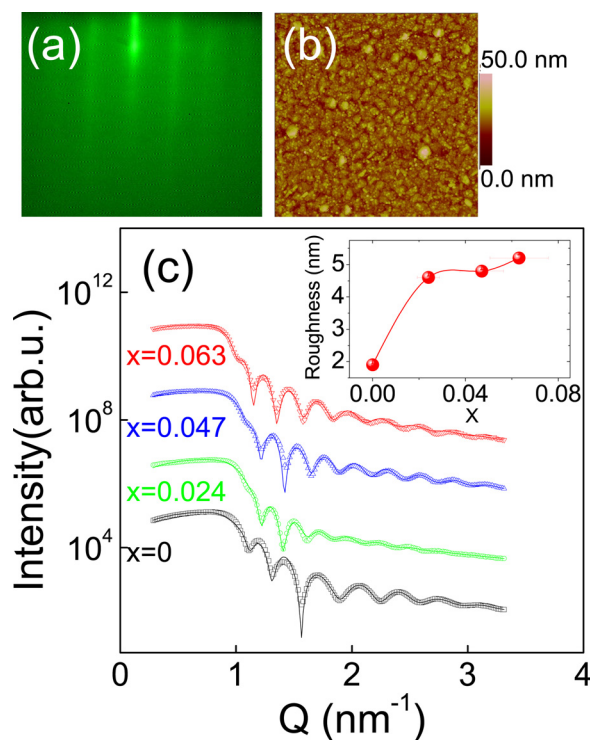
FIG. 1. (a) RHEED pattern for the $x = 0.047$ sample immediately prior to capping by MgF_2. (b) *Ex-situ* AFM image (lateral length scale: 2 μm × 2 μm) of the $x = 0.047$ sample after MgF_2 capping. (c) Low angle x-ray reflectivity data for the $Bi_{2-x}Mn_xSe_3$ films as a function of momentum transfer Q. Circles are the data and curves are the corresponding fits. Inset: RMS roughness at the $Bi_{2-x}Mn_xSe_3/MgF_2$ interface obtained from fits to the x-ray reflectivity data. Curve is a guide to the eye.

Figure 1(c) shows the results of the XRR measurements. For the samples with larger Mn concentrations, the interface roughness at the $Bi_{2-x}Mn_xSe_3$/MgF$_2$ roughness was larger, so in order to model this an interface layer between the $Bi_{2-x}Mn_xSe_3$ and MgF$_2$ layers with a scattering coherence length equal to the average of the two materials was introduced. The fits to the data yielded $Bi_{2-x}Mn_xSe_3$ film thickness parameters of 31.5, 30.7, 29.3, 28.5 ± 0.2 nm with interface layer thicknesses of 0.9, 2.8, 3.4, 3.4 ± 0.1 nm for the $x = 0$, 0.024, 0.047, 0.063 samples, respectively. This is indicative of the increasing roughness as a function of increasing Mn concentration. The roughness obtained from the fits shown in Fig. 1(c) between the $Bi_{2-x}Mn_xSe_3$ and interface layer are plotted in the inset of Fig. 1(c). This is another way of quantitatively characterizing the increase of the surface roughness of the $Bi_{2-x}Mn_xSe_3$ film with increasing x. This roughness was consistent with the RMS roughness obtained from the AFM data.

XRD patterns for all samples are shown in Fig. 2(a). Using a hexagonal basis, the films were [001]-oriented and the calculated out-of-plane hexagonal lattice parameter, c, increased (Fig. 2(b)), while the in-plane lattice constant a (Fig. 2(c)) decreased with increasing x. The value of c was determined from the out-of-plane (00l) peaks (using a hexagonal basis), while the value of a was determined from the position of the (015) peak and the value of c. A similar increase in c with increasing Cr impurity concentration observed in $Bi_{2-x}Cr_xSe_3$ thin films[10] has been attributed to intercalated Cr. As discussed in more detail below, however, intercalation of Mn in the Mn-doped samples is unlikely in view of the simultaneous decrease in a and the analysis of the EXAFS data.

To investigate the structural disorder in the films, rocking curve scans of the (00.15) peak were performed. The rocking curves are shown in Fig. 3(a) and their corresponding calculated full width at half maximum (FWHM) values are indicated in Fig. 3(b). Because the FWHM was larger in the Mn-doped samples than in the pure sample, we conclude that crystallographic disorder increased with increasing Mn
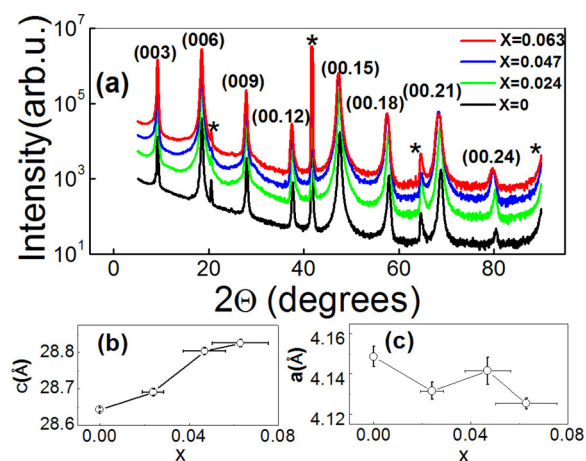
impurity level. Other 30 QL thick samples grown with $x > 0.063$ were not epitaxial; indeed, it was not possible to obtain RHEED or x-ray diffraction patterns for these samples which indicated that they were amorphous or polycrystalline. This trend is consistent with other work on Mn-doped Bi$_2$Se$_3$ (Refs. 25 and 26) and with measurements of $Bi_{2-x}Cr_xSe_3$ thin films, where the crystalline structure quickly deteriorated with increasing Cr doping.[10]

B. XPS measurements

XPS Bi 4f, Se 3d, and Mn 2p spectra are shown in Figs. 4(a), 4(b), and 4(c), respectively, for the 12 QL sample with $x = 0.13$ sample grown under the same conditions as the other samples described in the text. This sample had a larger Mn concentration which was desirable to obtain a larger Mn XPS signal, but the thickness was smaller in order to
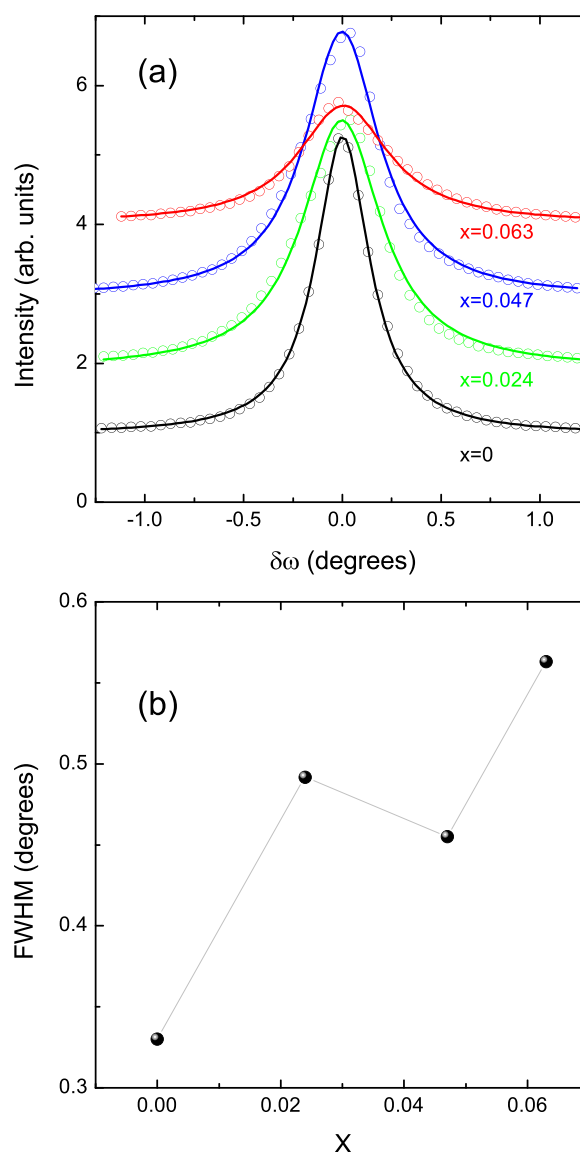
FIG. 3. (a) Rocking curves of the (00.15) x-ray diffraction peak for the samples uses in this study. The data have been offset along the vertical axis for clarity. The solid curves are fits to a Lorenzian peak function. (b) Full width at half maximum (FWHM) values obtained from the Lorenzian fits as a function x. The lines between data points are guides to the eye.

FIG. 2. (a) X-ray diffraction scans for $Bi_{2-x}Mn_xSe_3$ samples. The (00l) peaks are indicated using a hexagonal basis. Asterisks indicate substrate peaks. (b) Out-of-plane (001) lattice constant as a function of x. (c) In-plane (100) lattice constant as a function of x.

FIG. 4. XPS data (○) of Bi-4f (a), Se-3d (b), and Mn-2p (c) core levels for the 12 QL thick $x = 0.13$ sample. Data were acquired after sputtering off the MgF$_2$ capping layer as described in the text. The magenta curves represent the fit to Gaussian lineshapes which are shown by the red, blue, and green curves. The red and blue curves represent the electron spectra contributions of 4f$_{5/2}$ and 4f$_{7/2}$ for Bi, the 3d$_{3/2}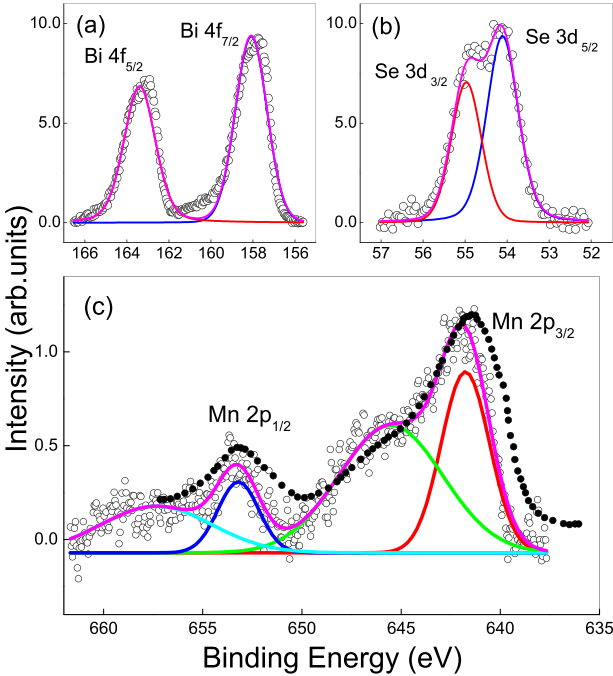$ and 3d$_{5/2}$ for Se, and 2p$_{3/2}$ and 2p$_{1/2}$ for Mn, respectively. For Mn (c), satellite peak contributions are also shown by the green and light blue curves. The black dots represent data for MnSe powder reported in Ref. 28.

preserve the Bi$_2$Se$_3$ crystal structure. After removing the background, the peaks arising from different transitions were fit to Gaussian lineshapes, with the total contributions of all transitions shown by the magenta curves in Fig. 4. The center of the peaks (binding energies E_B) and widths of the peaks determined from the fits are shown in Table I. Atomic concentrations of Mn were calculated by comparing the area under the curves of the Bi (Fig. 4(a)) and Mn (Fig. 4(c)) signals, and the calibration of the quartz crystal monitor was confirmed to be accurate to better than 20%.

For Bi 4f and Se 3d spectra, two peaks were observed which result from splitting due to spin-orbit coupling. The Bi 4f$_{7/2}$ and 4f$_{5/2}$ peaks were separated 5.4 eV (Fig. 4(a)) while the Se 3d$_{5/2}$ and 3d$_{3/2}$ separation was 0.9 eV (Fig. 4(b)), as

TABLE I. Results of analysis of XPS data using Gaussian lineshapes to determine the binding energy (E_B) and full width at half maximum (FWHM) of the peaks. The uncertainties for the peak position were no greater than ± 0.1 eV. The second peak for the Mn 2p signals is a satellite peak.

Core level	E_B (eV)	FWHM (eV)
Bi 4f$_{7/2}$	158.1	1.8
Bi 4f$_{5/2}$	163.4	1.5
Se 3d$_{5/2}$	54.0	0.8
Se 3d$_{3/2}$	54.9	1.0
Mn 2p$_{3/2}$	641.8	2.9
(satellite)	645.5	6.2
Mn 2p$_{1/2}$	653.2	2.4
(satellite)	657.3	6.6

expected from prior measurements performed for Bi$_2$Se$_3$ cleaved in vacuum.[27] The shoulder between the Bi 4f peaks is likely a result of the Se 3p$_{3/2}$ peak usually observed at $E_B \approx 160$ eV in Bi$_2$Se$_3$.[28,29]

The Mn 2p spectra provide valuable information regarding the Mn valence state. Figure 4(c) shows the multiplet splitting of the Mn-2p spectrum. The red and blue curves in Fig. 4(c) are the contributions to the 2p$_{3/2}$ and 2p$_{1/2}$ peaks, while the green and light blue curves are satellite peaks, resulting mostly from charge transfer effects between ligand p orbitals (in this case, the Se 3p orbitals, assuming bonding with Se nearest neighbors) and metal d orbitals (i.e., Mn 3d orbitals), which are commonly observed in transition-metal compounds.[30] The position of the 2p$_{3/2}$ peak at a binding energy $E_B = 641.8 \pm 0.1$ eV agrees well with the values found in the literature for Mn$_2$O$_3$ (641.7 eV) and MnSe (641.8 eV). Moreover, the separation between the main 2p$_{3/2}$ and 2p$_{1/2}$ peaks of 11.5 eV, resulting from spin-orbit coupling in the Mn atom, is in excellent agreement with data from Mn compounds.[28,30–32] The presence of broad satellite peaks at $E_B = 645.5$ and 657.3 eV is considered a reference for the presence of Mn^{2+}, which has been observed in MnO,[31] MnTe,[33] and MnSe,[28] but not in Mn$_2$O$_3$,[32] which is a Mn^{3+} compound. In Fig. 4(c), we also plot data for MnSe powder digitized from Ref. 28 (background not removed). Clearly, our data are very similar to the MnSe data in terms of the positions of the main and satellite Mn 2p peaks. The shoulder in the MnSe data near 640 eV likely comes from MnSe$_2$ impurities, since the 2p$_{3/2}$ peak for MnSe$_2$ is known to occur at 640.5 eV.[34] The position of the Mn peak in our sample at 641.8 eV, together with an absence of a shoulder at 640.5, is strong evidence that Mn in our Bi$_{2-x}$Mn$_x$Se$_3$ is in the Mn^{2+} state. We note that recent x-ray absorption spectroscopy work on Cr-doped Bi$_2$Se$_3$ indicates that Cr impurities also tend to be in the divalent state, in agreement with our results.[35]

C. X-ray absorption spectroscopy

EXAFS measurements were performed on the $x = 0.063$ sample to determine the specific lattice site(s) where the Mn atoms are absorbed. Data were analyzed using the Artemis software[36] to fit the first two shells, with initial geometry derived from the undistorted crystal structure.[37] Fits were done on the real space Fourier transform $\chi(R)$ of the response $k^3\chi(k)$ performed in the range of $2.5 < k < 10.0$ Å^{-1}.

The data for the magnitude and real part of $\chi(R)$ are shown in Figs. 5(a) and 5(b), respectively. We considered three possibilities: Mn going substitutionally in the Bi sites, Mn going into a Se site, and Mn cluster formation. For the Mn in the Bi site model, Se1.1 and Se2.1 refer to the Se1 and Se2 nearest neighbors of a Bi atom, corresponding to the Se1 and Se2 sites shown in Fig. 5(c). The best fitting results to $\chi(R)$ are represented by the curves in Fig. 5 with parameters shown in Table II. For Mn in the Se1 site, only nearest neighbor Bi sites were taken into account. For the case of Mn in Bi sites (red curves), the data were fit very well by including scattering from the Se1 and Se2 sites, with an R-factor of 0.0031. Interestingly, the data indicate that the
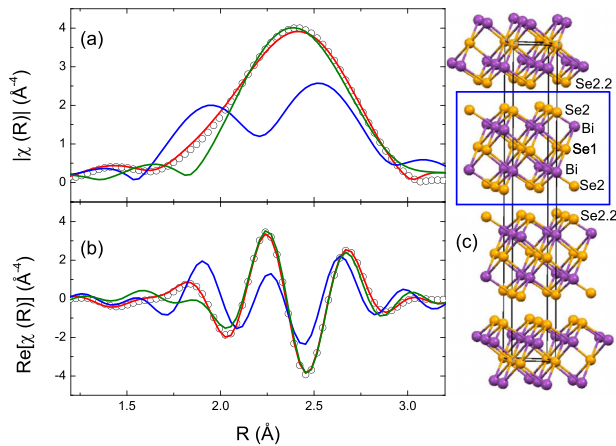
FIG. 5. EXAFS Fourier transform function $\chi(R)$ of the response function $k^3\chi(k)$ near the Mn Kα absorption edge for the $x = 0.063$ sample in the range of 1.2 Å to 3.2 Å. The results of the best fits to the magnitude (a) and real part (b) of $\chi(R)$ are shown for the Mn atom in the Bi and Se1 sites (red and blue curves, respectively). The case of possible metallic Mn clustering corresponds to the green curve. The unit cell corresponding to three Bi$_2$Se$_3$ QLs is shown in (c). A single QL is outlined by the blue square and the Bi and Se atomic sites, composed of layers along the (vertical) c-axis are indicated. Note that the Se1 and Se2 sites are inequivalent. The Se2.2 sites are Se2 sites in adjacent QLs.

Se nearest neighbors are much closer than if the sites were occupied by Bi. The Mn in Se1 site fit (blue curve) was qualitatively different from the data, showing a dip near the first-shell maximum characteristic of a Ramsauer-Townsend resonance resulting from scattering from the heavy Bi atoms (a similar result is obtained for substitution in the Se2 site).[38] For the Mn cluster model, the results indicate an anomalously low scattering amplitude ($S_0^2 = 0.18$). Moreover, although the shape of the main peak appears to be approximately correct, the structure around it is not reproduced by this model in terms of the positions of the secondary maxima and minima. This leads to an R-factor that is significantly higher than for the Mn in Bi site model (0.051). Therefore, our results support doping into the group V element site, in agreement with a previous EXAFS study of Mn-doped GaAs,[39] and disprove the Mn segregation scenario. Our results are in agreement with recent EXAFS work on Cr-doped Bi$_2$Se$_3$ single crystals where Cr was found to

substitute primarily into the Bi sites with a significant local contraction of the Cr-Se bond (2.50 Å).[40]

The Mn-Se bond lengths obtained from EXAFS were shorter than those corresponding to Bi-Se bonds in undoped Bi$_2$Se$_3$ (R and R_e, respectively, listed in Table II). In order to determine whether the bond lengths corresponding to the nearest neighbor paths determined from EXAFS are sensible, first-principles DFT calculations were performed using the Vienna *Ab-initio* Simulation Package (VASP)[42,43] which uses pseudopotentials together with the projector augmented wave approach. Starting with undoped Bi$_2$Se$_3$ lattice parameters $a = 4.138$ Å and $c = 28.64$ Å, the unit cell was relaxed to obtain the minimum energy geometry. The forces on each of the atoms were calculated using the Hellmann-Feynman theorem and were subsequently used to perform a conjugate gradient structural relaxation. The structural optimizations were continued until the forces on the atoms converged to less than 1 meV/Å. This optimization was completely carried through for both undoped and doped materials. A sufficiently high-energy cutoff of 350 eV was used in each calculation to obtain accurate results. The relaxed geometry of undoped Bi$_2$Se$_3$ yielded $a = 4.184$ Å and $c = 30.84$ Å. The calculated distance between first nearest Se-Bi neighbors was 2.88 Å and 3.00 Å, which are within 3% of the experimental values determined for single crystals of 2.85 Å and 3.07 Å, respectively.[37] The reason that the calculated lattice parameter disagreed significantly along the c-axis is the difficulty of the theory in calculating the Van der Waals interaction between adjacent Se-Se planes, but otherwise the bond length calculations were quite similar to our experimental observation. For the case of the Mn-doped system, we used a $2 \times 2 \times 1$ supercell and replaced one out of 24 Bi atoms by a Mn atom, as shown in Fig. 6(a), corresponding to $x = 0.084$. The lattice constants obtained for the Mn-doped structure were
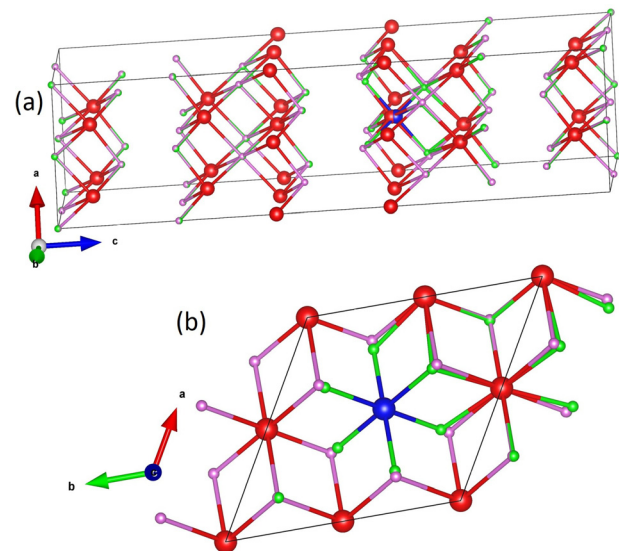
TABLE II. Results of fits to EXAFS data for 1.2 Å $< R <$ 3.2 Å. For the Mn in Bi site, only nearest Se atoms at Se2 and Se1 sites were considered, while for the Mn in Se1 site, only the nearest Bi sites were taken into account. The parameters S_0^2 and R are the amplitudes and shell distances obtained from the fits, while N and R_e are the expected degeneracy for each shell (number of atoms) and bond distances for the Bi$_2$Se$_3$ structure,[37] respectively (not fitting parameters). For the Mn cluster model, the shortest bond distance for the α-Mn structure is listed.[41] The Debye-Waller scattering factor σ^2 was a fitting parameter for the fits using the Mn in Bi and Mn cluster models. The number of equivalent scatterers N was left as a fixed value during the fitting process. Uncertainties are as reported by Artemis.

Site	R-factor	Path	N	σ^2 (Å^2)	S_0^2	R (Å)	R_e (Å)
Bi	0.0031	Se2.1	3	0.013 ± 0.007	0.9 ± 0.2	2.66 ± 0.03	2.851
		Se1.1	3	0.013 ± 0.006	0.9 ± 0.2	2.78 ± 0.03	3.075
Se1	0.53	Bi	6	0.025	0.1 ± 0.2	2.44 ± 0.03	3.074
Mn cluster	0.051	Mn	12	0.008 ± 0.003	0.18 ± 0.05	2.80 ± 0.02	2.752

FIG. 6. (a) Unit cell used for the DFT calculations. Red spheres are Bi atoms, magenta spheres are Se atoms corresponding to pure Bi$_2$Se$_3$, green spheres are Se atoms corresponding to Bi$_{2-x}$Mn$_x$Se$_3$, and the blue sphere is a Mn atom. The doped and undoped structures are superimposed to show the difference between them. (b) Perspective along the [001] direction (c-axis) of the quintuple layer containing the Mn impurity. Visualization rendered using the VESTA software package.[46]

$a = 4.173$ Å and $c = 30.89$ Å. Our calculations indicated that the Bi-Se bond lengths were 2.68 Å and 2.75 Å, as shown in Fig. 6(b), which agree well with the values of 2.66 Å and 2.78 Å determined from EXAFS data (Table II). These results were also consistent with recent DFT calculations of the structure of Mn and other transition metal impurities near the surface of Bi_2Se_3 (not in the bulk), which found bond lengths of 2.60 Å and 2.70 Å for Mn in Bi sites just below the surface.[18] Those same calculations determined that the energies of other configurations, including interstitial sites for Mn, are energetically unfavorable, and moreover, the calculated bond lengths from these other configurations were significantly different from the EXAFS values.[18] Finally, the EXAFS results are also consistent with Mn-Se bond lengths in MnSe and $MnSe_2$ (2.71 Å and 2.73 Å, respectively),[19] thus providing additional evidence that, in our samples, the Mn atoms are predominantly incorporated substitutionally into the Bi sites.

We note that in Cu-doped Bi_2Se_3 single crystals, Cu can be absorbed either substitutionally into the Bi sites or in positions intercalated between two adjacent Se van der Waals-bonded layers.[44] Intercalation of Cu impurities in single crystals can lead to superconductivity,[44] and in Cu-doped thin films, it has been recently found that Cu is absorbed in intercalated or interstitial sites.[45] In Cr-doped thin films, it has been argued that an expansion of the c-axis with increasing Cr doping is consistent with Cr being incorporated in intercalated sites.[10] Although we also observed an expansion in the c-axis with increasing Mn doping, the a-axis contracted by a similar amount, as shown in Figs. 2(b) and 2(c). In other words, the volume of the unit cell remained approximately constant. Together with the fact that the EXAFS results were consistent with Bi-substitution by Mn atoms, we conclude that the expansion along the c-axis was most likely not a result of Mn-intercalation. In fact, the a-axis was measured in only one of the Cr-doped films in Ref. 10, which was found to be smaller than the pure sample, so Cr intercalation may not occur in Cr-doped samples either. It is possible that the expansion along the c-axis is a result of the Mn impurities weakening the Van der Waals interaction between adjacent Se layers. Our experimental data indicate that the a-axis of the $x = 0.063$ sample contracted by 0.6% and the c-axis expanded by 0.7% with respect to the pure sample, while the DFT calculations yielded a contraction of 0.3% for the a-axis and an expansion of 0.2% for the c-axis. Although the DFT calculations gave the correct qualitative trend of the experimental data (a contraction of the a-axis and an expansion of the c-axis), the disagreement in the magnitudes may lie in the difficulty of calculating the van der Waals interaction using *ab-initio* methods. We therefore conclude that the changes in lattice parameters with Mn doping observed in our x-ray diffraction data are also consistent with Mn being substituted for Bi in the Bi_2Se_3 lattice.

D. Transport measurements

The longitudinal film resistivity ρ_{xx} was measured as a function of temperature in zero field as shown in Fig. 7(a). The resistivity of the film with $x = 0.063$ was approximately
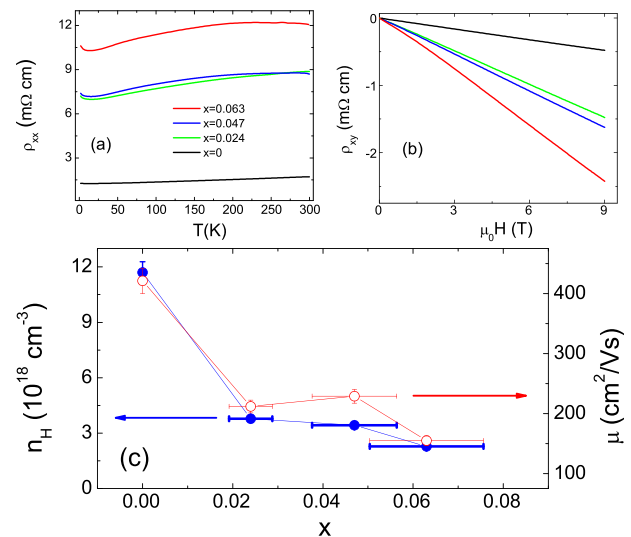

FIG. 7. (a) Temperature dependence of longitudinal resistivities. (b) Hall resistivity data at $T = 2$ K for different Mn concentrations as a function of magnetic field. (c) Charge carrier density n_H and mobility μ as functions of Mn-doping concentration.

an order of magnitude larger than the resistivity of the undoped sample, as expected from the increased scattering from magnetic Mn impurities and a larger density of structural defects. Temperature dependences had a strong metallic character for all samples at high temperatures. At temperatures below 15 K, however, the resistivity of all samples increased as the temperature was lowered. Similar findings have been reported[47] for Bi_2Se_3 films with thickness $t \leq 10$ QL, which have been explained by the Altshuler-Aronov-Lee (AAL) mechanism[48] where weak disorder results in a non-local effective enhanced electron-electron interaction.

Carrier densities, n_H, were calculated from the linear slopes of the corresponding Hall resistivities measured at $T = 2$ K shown in Fig. 7(b). All samples had n-type carriers and the bulk charge carrier density decreased with increasing Mn concentration, as shown in Fig. 7(c). This indicates that the Mn impurities acted as acceptors that compensated the bulk carriers. This compensation could occur if the valence of Mn was 2+ instead of 3+, which is consistent with the structural data discussed above. The mobilities were calculated using the standard equation $\mu = (e\rho_{xx}n_H)^{-1}$, where e is the charge of the electron. The decrease in mobility with increasing Mn-doping, shown in Fig. 7(c), is due to the increased electron scattering from defects.

It is important to note that the decrease in the number of carriers with increasing Mn concentration is modest (a factor of three) and much lower than expected if all of the Mn sites acted as acceptors. However, the structural data indicate that incorporation of Mn also adds structural defects, possibly grain boundaries and/or Se vacancies, for example. These structural defects could have the opposite effect, adding carriers to the conduction band at the same time that the Mn sites act as acceptors. Therefore, the acceptors introduced by Mn^{+2} substitution into Bi sites is compensated in large part by donors resulting from other structural defects induced by Mn incorporation into the lattice.

IV. CONCLUSIONS

$Bi_{2-x}Mn_xSe_3$ thin films were grown using molecular beam epitaxy and their structure was systematically investigated using x-ray diffraction, x-ray reflectivity, XPS, and EXAFS. The structural quality of the samples was maintained for 30 QL thick samples with $x \leq 0.063$. It was verified that the Mn atoms were incorporated substitutionally into the Bi sites with a Mn^{+2} valence using XPS, EXAFS, and DFT calculations. No evidence of intercalated incorporation of Mn was found, unlike Cu-Bi_2Se_3, where both intercalation and substitutional incorporations have been identified. The behavior of the electrical resistivity and mobility as a function of temperature was consistent with Mn impurities acting as acceptors for Mn substitution in Bi sites. Structural defects created by Mn incorporation result in additional donors that mitigate the compensation effects due to Mn^{2+} acceptors.

ACKNOWLEDGMENTS

[1]L. Fu and C. L. Kane, Phys. Rev. B **76**, 045302 (2007).

[2]M. Z. Hasan and C. L. Kane, Rev. Mod. Phys. **82**, 3045 (2010).

[3]J. E. Moore, Nature **464**, 194 (2010).

[4]D. Hsieh, D. Qian, L. Wray, Y. Xia, Y. S. Hor, R. J. Cava, and M. Z. Hasan, Nature **452**, 970 (2008).

[5]Z.-H. Pan, E. Vescovo, A. V. Fedorov, D. Gardner, Y. S. Lee, S. Chu, G. D. Gu, and T. Valla, Phys. Rev. Lett. **106**, 257004 (2011).

[6]C. Jozwiak, Y. L. Chen, A. V. Fedorov, J. G. Analytis, C. R. Rotundu, A. K. Schmid, J. D. Denlinger, Y.-D. Chuang, D.-H. Lee, I. R. Fisher, R. J. Birgeneau, Z.-X. Shen, Z. Hussain, and A. Lanzara, Phys. Rev. B **84**, 165113 (2011).

[7]H. Zhang, C.-X. Liu, X.-L. Qi, X. Dai, Z. Fang, and S.-C. Zhang, Nat. Phys. **5**, 438 (2009).

[8]J. J. Cha, M. Claassen, D. Kong, S. S. Hong, K. J. Koski, X.-L. Qi, and Y. Cui, Nano Lett. **12**, 4355 (2012), see http://pubs.acs.org/doi/pdf/10.1021/nl3021472.

[9]M. Liu, J. Zhang, C.-Z. Chang, Z. Zhang, X. Feng, K. Li, K. He, L.-l. Wang, X. Chen, X. Dai, Z. Fang, Q.-K. Xue, X. Ma, and Y. Wang, Phys. Rev. Lett. **108**, 036805 (2012).

[10]P. P. J. Haazen, J.-B. Laloë, T. J. Nummy, H. J. M. Swagten, P. Jarillo-Herrero, D. Heiman, and J. S. Moodera, Appl. Phys. Lett. **100**, 082404 (2012).

[11]J.-M. Zhang, W. Zhu, Y. Zhang, D. Xiao, and Y. Yao, Phys. Rev. Lett. **109**, 266405 (2012).

[12]Y. H. Choi, N. H. Jo, K. J. Lee, H. W. Lee, Y. H. Jo, J. Kajino, T. Takabatake, K.-T. Ko, J.-H. Park, and M. H. Jung, Appl. Phys. Lett. **101**, 152103 (2012).

[13]S.-Y. Xu, M. Neupane, C. Liu, D. Zhang, A. Richardella, L. Andrew Wray, N. Alidoust, M. Leandersson, T. Balasubramanian, J. Sanchez-Barriga, O. Rader, G. Landolt, B. Slomski, J. Hugo Dil, J. Osterwalder, T.-R. Chang, H.-T. Jeng, H. Lin, A. Bansil, N. Samarth, and M. Z. Hasan, Nat. Phys. **8**, 616 (2012).

[14]D. Zhang, A. Richardella, D. W. Rench, S.-Y. Xu, A. Kandala, T. C. Flanagan, H. Beidenkopf, A. L. Yeats, B. B. Buckley, P. V. Klimov, D. D. Awschalom, A. Yazdani, P. Schiffer, M. Z. Hasan, and N. Samarth, Phys. Rev. B **86**, 205127 (2012).

[15]H. J. von Bardeleben, J. L. Cantin, D. M. Zhang, A. Richardella, D. W. Rench, N. Samarth, and J. A. Borchers, Phys. Rev. B **88**, 075149 (2013).

[16]S. Hikami, A. I. Larkin, and Y. Nagaoka, Prog. Theor. Phys. **63**, 707 (1980), see http://ptp.oxfordjournals.org/content/63/2/707.full.pdf+html.

[17]H.-Z. Lu and S.-Q. Shen, Phys. Rev. B **84**, 125138 (2011).

[18]L. B. Abdalla, L. Seixas, T. M. Schmidt, R. H. Miwa, and A. Fazzio, Phys. Rev. B **88**, 045312 (2013).

[19]A. J. Jacobson and B. E. F. Fender, J. Chem. Phys. **52**, 4563 (1970).

[20]N. Bansal, Y. S. Kim, M. Brahlek, E. Edrey, and S. Oh, Phys. Rev. Lett. **109**, 116804 (2012).

[21]P. Tabor, C. Keenan, S. Urazhdin, and D. Lederman, Appl. Phys. Lett. **99**, 013111 (2011).

[22]Y. D. Glinka, S. Babakiray, T. A. Johnson, A. D. Bristow, M. B. Holcomb, and D. Lederman, Appl. Phys. Lett. **103**, 151903 (2013).

[23]M. Björck and G. Andersson, J. Appl. Crystallogr. **40**, 1174 (2007).

[24]M. A. Marcus, A. A. MacDowell, R. Celestre, A. Manceau, T. Miller, H. A. Padmore, and R. E. Sublett, J. Synchrotron Radiat. **11**, 239 (2004).

[25]J. A. Hagmann, "Magnetotransport investigation of bismuth chalcogenide topological insulators," Ph.D. dissertation (University of Notre Dame, Notre Dame, Indiana, USA, 2013).

[26]L. J. Collins-McIntyre, M. D. Watson, A. A. Baker, S. L. Zhang, A. I. Coldea, S. E. Harrison, A. Pushp, A. J. Kellock, S. S. P. Parkin, G. van der Laan, and T. Hesjedal, AIP Adv. **4**, 127136 (2014).

[27]D. Kong, J. J. Cha, K. Lai, H. Peng, J. G. Analytis, S. Meister, Y. Chen, H.-J. Zhang, I. R. Fisher, Z.-X. Shen, and Y. Cui, ACS Nano **5**, 4698 (2011), see http://dx.doi.org/10.1021/nn200556h.

[28]A. Mandale, S. Badrinarayanan, S. Date, and A. Sinha, J. Electron Spectrosc. Relat. Phenom. **33**, 61 (1984).

[29]V. A. Golyashov, K. A. Kokh, S. V. Makarenko, K. N. Romanyuk, I. P. Prosvirin, A. V. Kalinkin, O. E. Tereshchenko, A. S. Kozhukhov, D. V. Sheglov, S. V. Eremeev, S. D. Borisova, and E. V. Chulkov, J. Appl. Phys. **112**, 113702 (2012).

[30]F. de Groot and A. Kotani, *Core Level Spectroscopy of Solids* (CRC Press, Boca Raton, FL, 2008).

[31]M. A. Langell, C. W. Hutchings, G. A. Carson, and M. H. Nassir, J. Vac. Sci. Technol., A **14**, 1656 (1996).

[32]M. A. Stranick, Surf. Sci. Spectra **6**, 39 (1999).

[33]R. Iwanowski, M. Heinonen, and E. Janik, Chem. Phys. Lett. **387**, 110 (2004).

[34]H. van der Heide, R. Hemmel, C. van Bruggen, and C. Haas, J. Solid State Chem. **33**, 17 (1980).

[35]A. I. Figueroa, G. van der Laan, L. J. Collins-McIntyre, S.-L. Zhang, A. A. Baker, S. E. Harrison, P. Schönherr, G. Cibin, and T. Hesjedal, Phys. Rev. B **90**, 134402 (2014).

[36]B. Ravel and M. Newville, J. Synchrotron Radiat. **12**, 537 (2005).

[37]S. Nakajima, J. Phys. Chem. Solids **24**, 479 (1963).

[38]R. B. Brode, Rev. Mod. Phys. **5**, 257 (1933).

[39]F. d'Acapito, G. Smolentsev, F. Boscherini, M. Piccin, G. Bais, S. Rubini, F. Martelli, and A. Franciosi, Phys. Rev. B **73**, 035314 (2006).

[40]Z. Liu, X. Wei, J. Wang, H. Pan, F. Ji, F. Xi, J. Zhang, T. Hu, S. Zhang, Z. Jiang, W. Wen, Y. Huang, M. Ye, Z. Yang, and S. Qiao, Phys. Rev. B **90**, 094107 (2014).

[41]C. P. Gazzara, R. M. Middleton, R. J. Weiss, and E. O. Hall, Acta Crystallogr. **22**, 859 (1967).

[42]G. Kresse and J. Hafner, Phys. Rev. B **47**, 558 (1993).

[43]G. Kresse and J. Furthmüller, Phys. Rev. B **54**, 11169 (1996).

[44]Y. S. Hor, A. J. Williams, J. G. Checkelsky, P. Roushan, J. Seo, Q. Xu, H. W. Zandbergen, A. Yazdani, N. P. Ong, and R. J. Cava, Phys. Rev. Lett. **104**, 057001 (2010).

[45]M. Brahlek, N. Koirala, M. Salehi, N. Bansal, and S. Oh, Phys. Rev. Lett. **113**, 026801 (2014).

[46]K. Momma and F. Izumi, J. Appl. Crystallogr. **44**, 1272 (2011).

[47]M. Liu, C.-Z. Chang, Z. Zhang, Y. Zhang, W. Ruan, K. He, L.-L. Wang, X. Chen, J.-F. Jia, S.-C. Zhang, Q.-K. Xue, X. Ma, and Y. Wang, Phys. Rev. B **83**, 165440 (2011).

[48]B. L. Altshuler, A. G. Aronov, and P. A. Lee, Phys. Rev. Lett. **44**, 1288 (1980).